*Zebb Prime, Danielle J. Moreauy and Con J. Doolan
Flow modelling and noise generation of interacting prisms
20th AIAA/CEAS Aeroacoustics Conference, 2014 / pp.2014-3287-1-2014-3287-19

AIAA Aviation
16-20 June 2014, Atlanta, GA
20th AIAA/CEAS Aeroacoustics Conference

Flow modelling and noise generation of interacting prisms

Zebb Prime*, Danielle J. Moreau†, and Con J. Doolan‡
The University of Adelaide, South Australia, Australia 5005
Mohamed Sukri Mat Ali§, Sufiah Mohd Salleh ¶, and Siti Nur Aishah Mohd Haris‖
Malaysia-Japan International Institute of Technology (MJIIT), Universiti Teknologi Malaysia, Malaysia 54100

Noise generation is a significant issue for High-Speed Trains (HSTs), and as speeds increase aerodynamically generated noise becomes the dominant noise source. In this article, the effect of nose shape, carriage separation and yaw angle on the aerodynamics and noise generation are analysed using two prisms, representing a HST model. The aerodynamics are modelled using Computation Fluid Dynamics (CFD), and the flow velocity and turbulence intensity in various positions in the wake are compared with experimental hotwire data measured in the Anechoic Wind Tunnel (AWT) at The University of Adelaide, with good agreement. Finally, acoustic beamforming images of the noise generated by the interacting prisms measured in the AWT are presented. The acoustic results show that a blunt nose tends to increase noise at lower frequencies significantly, while increasing prism separation tends to increase noise over most frequencies, but most significantly at mid-frequencies, and increasing yaw angle increases noise across all frequencies. Beamforming results show that at lower frequencies, this noise tends to be generated at the leading and trailing edges, while at higher frequencies the noise tends to be generated in the carriage gap.

I. Introduction

Many countries have turned to High-Speed Trains (HSTs) as a means of increasing transport capacity and reducing travel times along high-traffic routes. However noise generation is one of the factors preventing further improvements in operating speeds.[1]

Noise generated by traditional trains is usually dominated by mechanical noise, such as rolling, however at higher speeds aerodynamically generated noise becomes the strongest noise source.[2,3,4] The main aerodynamic noise sources include the pantograph, the inter-coach spacing and the nose of the leading car.[4]

This work aims to investigate the noise generation of flow over two prisms, representing a model HST, with varying nose geometry, inter-carriage spacing and yaw angle using a combination of aerodynamic modelling and analysis using Computational Fluid Dynamics (CFD), and aeroacoustic beamforming.

The study on train aerodynamics is growing with the help of numerical simulations and various experimental methods. Example of researchers who have experimentally measured the train aerodynamics are Baker et al.,[5] Chiu and Squire,[6] Copley,[7] Suzuki et al[8] and Hoppmann.[9] Their investigations focussed on the aerodynamic characteristics such as drag, lift and side force together with the measurement of flow characteristics along the train. Chiu et al[6] investigated the effect of yaw angle on the formation of vorticies through full scale wind tunnel experiments. They found that at yaw angles up to 45°, vortices are formed like those found on slender bodies. Copley[7] found little separation near the nose of train at 25° yaw, and little effect on the wake downstream of the train. For a yaw angle range of 40°–60°, the increase in the roll

*Research Associate, School of Mechanical Engineering, zebb.prime@adelaide.edu.au, AIAA member
†Research Associate, School of Mechanical Engineering, danielle.moreau@adelaide.edu.au, AIAA member
‡Associate Professor, School of Mechanical Engineering, con.doolan@adelaide.edu.au, AIAA Senior member
§Senior Lecturer, Department of Mechanical Precision Engineering, sukri@ic.utm.my, AIAA Senior member
¶Student,Department of Mechanical Precision Engineering, sufiahsalleh90@gmail.com
‖Student,Department of Mechanical Precision Engineering, sn.aishah@gmail.com

moment stops due to the breakdown of the lee-vortex.[10] This shows that the flow structure around a HST is significantly influenced by the yaw angle.

Suzuki et al[8] investigated that effect of roof geometry on the side force acting perpendicular to vehicles. He found that the side force coefficient increases more as the roof of the vehicles became 'edgier'. Four types of roof were investigated and it was found that a round roof has the lowest side force because a negative pressure area develops on the roof of the train. Copley[7] investigated the effect of Reynolds number on the flow field around a train subjected to crosswinds. For low Reynolds number, flow around train is laminar and remain attached to the train surface. At high Reynolds numbers, the flow become turbulent in the wake and reattaches to the roof of the train.

CFD has improved the design cycle of HSTs, as it allows rapid iteration of designs without the material cost of building models. However, to solve all the scales of the full flow field around a train is too computational demanding.[11] There are three dominant turbulence models used in HST numerical simulations: direct numerical simulation (DNS), Reynolds Averaged Navier-Stokes (RANS), and Large Eddy Simulation (LES).[12] DNS is not suitable for HSTs because the turbulent scales become smaller as the Reynolds number increases. Modern CFD methods based on RANS and turbulence model of $k-\epsilon$ have been applied to trains since the early 1990s. The TRANSAERO program uses RANS-based CFD with a renormalization group theory (RNG) $k-\epsilon$ turbulence model. An intermediate method between DNS and RANS is LES that can resolve large scale of the turbulence and model the small scale of turbulence.

Current development work on HSTs has focussed on the geometry of the train model, especially on the first car. The first car plays an important role in train stability and noise generation because it is exposed to the strongest wind forces and moments.[12,13] Bilal et al[14] showed that a HSTs crosswind aerodynamic coefficients heavily depend on train shape and infrastructure configuration. The influence of nose shape has been investigated by Hemida et al[15] by comparing the flow structure between two types of nose shapes: a long nose model and a short nose model, with the short nose model generating more vortex structures in the wake.

Beamforming is an array signal processing technique often used in acoustics to identify and/or enhance noise sources. This technique has often been used on HSTs to identify noise sources, which identify the above mentioned aerodynamic noise sources[2,16] as well as rolling noise being the most significant noise sources.[2,4,17]

This paper presents recent results of investigating the effect of nose geometry, inter-carriage spacing and yaw angle on the noise generation of two prisms. The paper is structured as follows, the CFD and experimental methodologies are presented in Section II, followed by CFD results, a comparison of the CFD and hotwire results, and the acoustic and beamforming results in Section III. Conclusions and intended further work are finally discussed in Section IV.

II. Apparatus and methodology

A. Prisms

The prisms representing a HST model consists of a leading prism with three replaceable noses; a square nose, triangular nose, and a elliptical (termed rounded) nose, and a trailing prism. The prisms have a square cross-section with sides $D = 15\,\text{mm}$. The leading prism is $3D$ long (without a nose), the trailing prism is $4D$ long, the square and triangular noses are $1D$ long while the elliptical nose is $1.5D$ long, as shown in Figure 1.

B. Numerical Simulation

For the numerical simulation, only the case of square nose shape with a gap between the prisms of $0.5D$ and a yaw angle of zero degree is considered. Cases with different nose geometry, prism spacing and yaw angles will be presented in future work.

1. Computational Domain

The computational domain used in this study is shown in Figure 2. Uniform free stream velocity and zero pressure gradient are set at the inlet located $10D$ upstream from the leading edge of the upstream body. The outlet is $20D$ downstream from the trailing edge of the downstream body, where zero velocity gradient and fixed ambient pressure conditions are set. The ground is defined as a wall with slip condition and zero

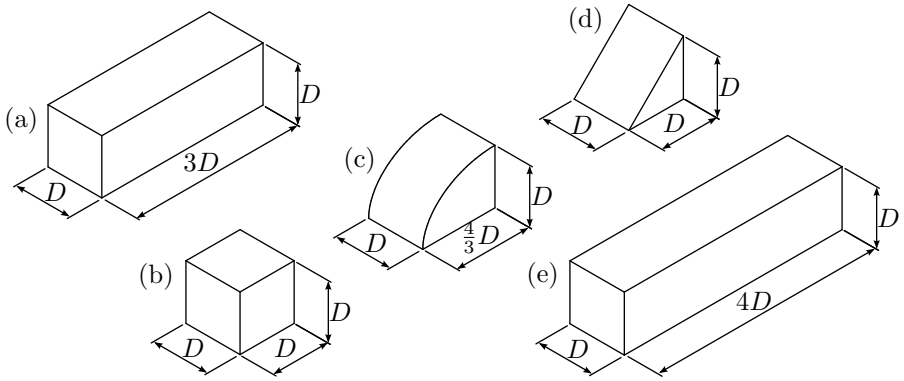

Figure 1: Prism components, representing a HST model, with $D = 15\,\text{mm}$. (a) Front car, (b) Square nose, (c) Rounded nose, (d) Triangular nose, and (e) Rear car.

pressure gradient. The distance between the bottom surfaces of the trains and the ground is $1.5D$, a 15% higher than the experimental setup, described below in Section C.

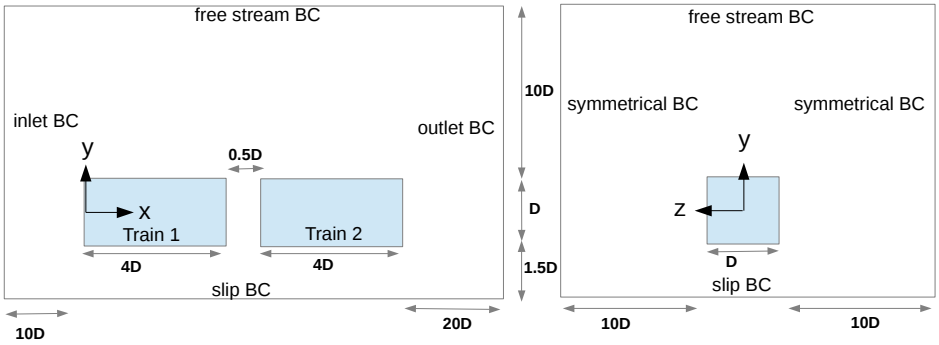

Figure 2: Sketch of the problem geometry and flow domain for the flow simulations (not to scale).

2. Governing equations and solution method

Calculations are carried using the unsteady Reynolds Navier Stokes (URANS) and continuity equations:

$$\rho\frac{\partial U_i}{\partial t} + \rho U_j\frac{\partial U_i}{\partial x_j} = \frac{\partial}{\partial x_j}\left[-\bar{p}\delta_{ij} + \mu\left(\frac{\partial U_i}{\partial x_j} + \frac{\partial U_j}{\partial x_i}\right) - \rho\overline{u_i' u_j'}\right]. \tag{1}$$

$$\frac{\partial \rho}{\partial t} + (\rho U_i)_{,i} = 0 \tag{2}$$

where $\left(-\rho\overline{u_i' u_j'}\right)$ is the Reynolds stress.

The Reynolds stress is solved using an eddy-viscosity model based on the Boussinesq assumption;

$$-\rho\overline{u_i' u_j'} = \mu_t\left(\frac{\partial U_i}{\partial x_j} + \frac{\partial U_j}{\partial x_i} - \frac{2}{3}\frac{\partial U_k}{\partial x_k}\delta_{ij}\right) - \frac{2}{3}\rho k\delta_{ij} \tag{3}$$

where the turbulent kinetic energy (k) and and the specific dissipation rate are solved using the following equations;[18]

$$\frac{\partial k}{\partial t} + U_j \frac{\partial k}{\partial x_j} = P_k - \beta^* k\omega + \frac{\partial}{\partial x_j}\left[(\nu + \sigma_k \nu_T)\frac{\partial k}{\partial x_j}\right] \tag{4}$$

$$\frac{\partial \omega}{\partial t} + U_j \frac{\partial \omega}{\partial x_j} = \alpha S^2 - \beta \omega^2 + \frac{\partial}{\partial x_j}\left[(\nu + \sigma_\omega \nu_T)\frac{\partial \omega}{\partial x_j}\right] + 2(1 - F_1)\sigma_{\omega 2}\frac{1}{\omega}\frac{\partial k}{\partial x_i}\frac{\partial \omega}{\partial x_i} \tag{5}$$

where ν_T is kinematic eddy viscosity and it is defined as;

$$\nu_T = \frac{a_1 k}{\max(a_1 \omega, SF_2)} \tag{6}$$

The following closure coefficient is used in this study;

$$F_2 = \tanh\left[\left[\max\left(\frac{2\sqrt{k}}{\beta^* \omega y}, \frac{500\nu}{y^2 \omega}\right)\right]^2\right] \tag{7}$$

where y is the distance to the next surface,

$$P_k = \min\left(\tau_{ij}\frac{\partial U_i}{\partial x_j}, 10\beta^* k\omega\right) \tag{8}$$

$$F_1 = \tanh\left\{\left\{\min\left[\max\left(\frac{\sqrt{k}}{\beta^* \omega y}, \frac{500\nu}{y^2 \omega}\right), \frac{4\sigma_{\omega 2} k}{CD_{k\omega} y^2}\right]\right\}^4\right\} \tag{9}$$

$$CD_{k\omega} = \max\left(2\rho\sigma_{\omega 2}\frac{1}{\omega}\frac{\partial k}{\partial x_i}\frac{\partial \omega}{\partial x_i}, 10^{-10}\right) \tag{10}$$

$$\phi = \phi_1 F_1 + \phi_2(1 - F_1) \tag{11}$$

$$\alpha_1 = \frac{5}{9}, \alpha_2 = 0.44 \tag{12}$$

$$\beta_1 = \frac{3}{40}, \beta_2 = 0.0828, \beta^* = \frac{9}{100} \tag{13}$$

$$\sigma_{k1} = 0.85, \sigma_{k2} = 1, \sigma_{\omega 1} = 0.5, \sigma_{\omega 2} = 0.856 \tag{14}$$

The 2nd-order backward scheme[19] is used for temporal discretisation, the convection term is discretised using the 3rd-order QUICK scheme[20] and 2nd-order unbounded Gauss linear differencing scheme is used for the viscous term. The CFL number[21] is kept below 0.5. The OpenFOAM[22] numerical system that is based on the finite volume method is used to solve the governing equations.

A structured non-uniform Cartesion mesh is used to constructed the cells in the computational domain. Three grid resolutions have been assessed for its grid independent. Table. 1 shows the grid properties for each case. Wall functions have been used for all cases to reduce the computational cost and the accuracy of the calculations is maintained by keeping the cell size near the surface satisfies $10 < y^+ < 100$. Table. 2 and 3 compares the globals results obtained from the three grid resolutions. The changes in the results between the coarse grid and medium grid is more than one order of magnitude, but it reduces when the grid resolution is increased.

$$C_L = \frac{\text{Lift}}{\frac{1}{2}\rho U_\infty^2 A} \tag{15}$$

$$C_S = \frac{\text{Side}}{\frac{1}{2}\rho U_\infty^2 A} \tag{16}$$

Table 1: Grid resolution for the three types of mesh

Mesh	No. of Cells	Smallest cell size	y^+
Coarse	$2520 \times 2090 \times 1670$	$0.20D$	$47 < y^+ < 100$
Medium	$5020 \times 2780 \times 3305$	$0.11D$	$25 < y^+ < 87$
Fine	$7540 \times 3470 \times 4305$	$0.03D$	$17 < y^+ < 62$

Table 2: Global results for the upstream train

Mesh	$C_{L_{\text{rms}}}$	$C_{S_{\text{rms}}}$	$C_{D_{\text{mean}}}$
Coarse	0.00082	0.00056	0.71
Medium	0.00843	0.00614	0.74
Fine	0.08139	0.01161	0.78

$$C_D = \frac{\text{Drag}}{\frac{1}{2}\rho U_\infty^2 A} \tag{17}$$

where $A = D \times D$. Lift, Side and Drag are the aerodynamic forces in the direction upward, sideward and windward to the trains, respectively.

C. Anechoic wind tunnel facility

Acoustic beamforming and hotwire experiments were performed in the anechoic wind tunnel located at the University of Adelaide. The tunnel consists of a free-jet rectangular outlet of dimensions 75×275 mm with a maximum velocity of ≈ 40 m/s, and a free-stream turbulence intensity at the contraction outlet of 0.33 %.[23]

The tunnel outlet is located within an enclosure of internal dimensions $1.4 \times 1.4 \times 1.6$ m which has been acoustically treated with foam wedges. The enclosure provides a near reflection free environment above 250 Hz.

Mounted inside the enclosure are two sparse phased arrays, one above and one to the side of the outlet, for performing the beamforming measurements. Each array consists of 31 GRAS 40PH 1/4" array (phase matched) microphones arranged in an Underbrink[24] pattern. The top array has 5 arms each with 6 microphones with an arm spiral rate of $\nu = \frac{13}{32}$pi rad, maximum and minimum radius of $r_{\text{m}} = 0.49$ m and $r_0 = 0.04$ m with the final microphone located at the centre. The parameters of the side array are identical to the top array with the exception of the maximum radius, which is slightly less at $r_{\text{m}} = 0.45$ m.

With the cartesian coordinate system located at the centre of the outlet, and x being downstream, y to the left (while looking downstream), and z upward, the centre of the top array is located at $(0.357, 0, 0.51)$m, while the centre of the side array is located at $(0.325, 0.61, -0.06)$m.

The prisms were attached to a side-plate of size 300×155 mm which was slotted to allow for yaw angles up to 10° and prism separation ranging from $0D$ to $2D$.

The prisms were elevated above the side plate by two cylindrical posts of outer diameter 6 mm and length 22.5 mm to ensure the model was outside the boundary layer.

Table 3: Global results for the downstream train

Mesh	$C_{L_{\text{rms}}}$	$C_{S_{\text{rms}}}$	$C_{D_{\text{mean}}}$
Coarse	0.00049	0.00067	0.21
Medium	0.01152	0.00765	0.19
Fine	0.01149	0.01456	0.20

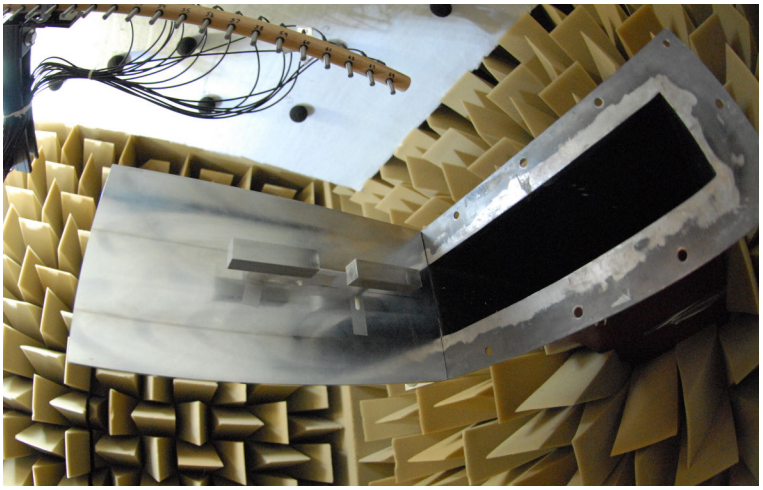

Figure 3: Train model with the square nose mounted to the side plate, which in turn is mounted to the wind tunnel outlet. Please note the visible line array was removed for this study.

D. Experimental method

Tests were performed on the train model for all combinations of noses, yaw angles of 0°, 5° and 10°, and car separations of $0D$, $0.5D$, $1D$, $1.5D$ and $2D$. All tests were performed at a constant flow speed of $U = 32\,\mathrm{m/s}$, for a Reynolds number based on D of $Re_D = 3.1 \times 10^4$.

During all experiments, exposed sections of slots were taped to prevent cavity noise generation, and a shroud was placed over the posts to prevent cylinder noise dominating the results.

For each test case microphone measurements from the two beamforming arrays were logged using using National Instruments PXIe-4499 24-bit simultaneous sample and hold ADCs cards at a sample rate of $2^{16}\,\mathrm{Hz}$ and for 10 s duration.

Averaged sound source contribution maps were constructed from each measurement by calculating the cross-spectrum matrix (or spatial correlation matrix) consisting of all pairs of array microphone cross-spectral estimates,[25] with diagonal removal[26] to reduce the influence of the self-noise in each channel. The cross-spectrum matrix was constructed by first high-pass filtering each microphone signal using a 256 element FIR filter designed using the window method with a cut-off frequency of 300 Hz, then calculating the cross-spectrum with every pair of microphones using a Hanning window and an FFT size of 2^{13} for a frequency resolution of 8 Hz.

The effect of acoustic path convection and refraction through the flow shear layer was accounted for by adjusting the source map by Mh, where M is the Mach number and h is the distance from the source to the shear layer, as shown in Ref. 27.

Hot-wire anemometry was used to obtain unsteady velocity data around the prisms. A TSI 1210-T1.5 single-wire probe with a wire length of $L = 1.27\,\mathrm{mm}$ and a wire diameter of $d = 3.81\,\mu\mathrm{m}$ was used. The sensor was connected to a TSI IFA300 constant temperature anemometer system and positioned using a Dantec automatic traverse with $6.25\,\mu\mathrm{m}$ positional accuracy. The traverse allowed continuous movement in the streamwise (x), spanwise (y), and vertical (z) directions. The velocity data were recorded using a National Instruments PCI-4472 board at a sampling frequency of 2^{16}Hz for a sample time of 10 s.

III. Results

A. Fluid dynamics

Figure 4 shows the magnitude of vorticity contours, $|\Omega D/U_\infty|$, where $\Omega = \nabla \times \mathbf{V}$ with $\mathbf{V}$ is the instantaneous velocity field. Similar to the case of flow over a square cylinder,[28,29] the flow separates at the front edge of the cylinder due to a sudden change in the geometry. Shear layers are generated that originate from each of the upstream edges and reattach about $1.5D$ downstream from the leading edge. Secondary flow detachments are observed at about $3D$ from the leading edge and they generate secondary shear layers that then hit

the leading edge of the downstream body. The structure and magnitude of the vorticity are approximately equal between the four side surfaces of the bodies, as shown in Figures 4a and 4b. This is expected as the axis of symmetry of these bodies is inline with the freestream velocity, where a different behaviour may be observed when different nose shapes (rounded and triangular) are used. However, the vorticity structures and strength change downstream, (see Figures 4c to 4e).

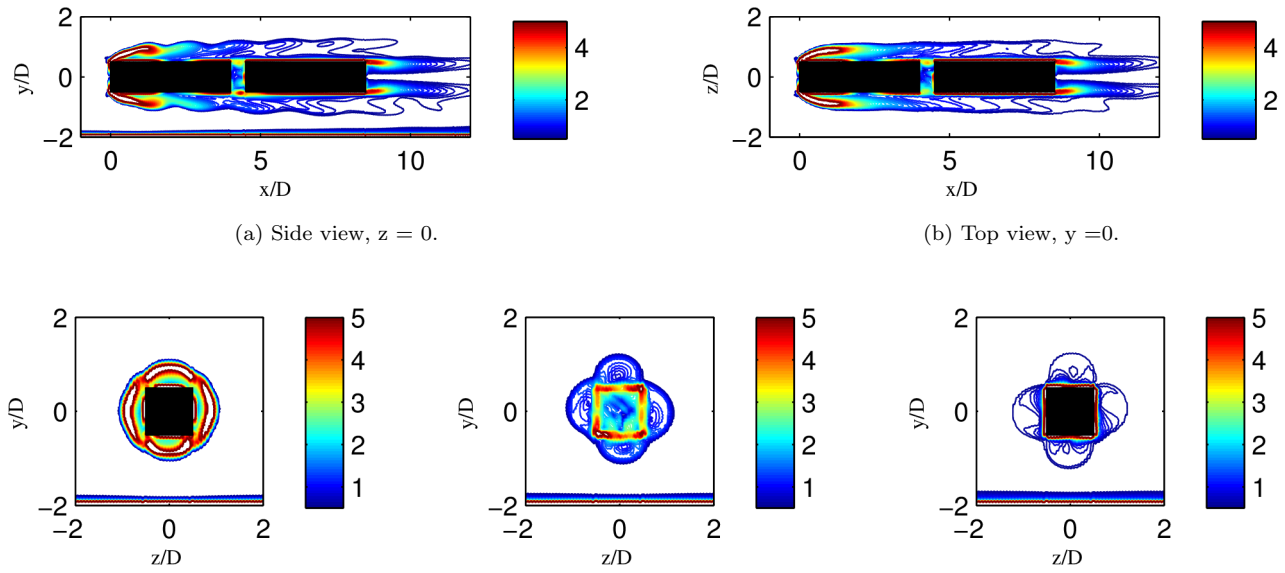

(a) Side view, z = 0.

(b) Top view, y =0.

(c) Front view, x = D.

(d) Front view, x = 4.25D.

(e) Front view, x = 8.5D.

Figure 4: Instantaneous vorticity magnitude ($|\Omega D/U_\infty|$) at various selected planes.

The leading and trailing edges vortices induce a strong pressure fluctuation, similar to the case of a two-dimensional flow over a rectangular cylinder.[30] This is shown in Figure 5. The stronger the vortex, the higher the pressure fluctuations that will be generated. However, near the leading edge of the upstream body, unlike the vorticity contour, the contour of the fluctuating pressure is not the same between the side surfaces and the top surfaces, as shown in Figures 5a and 5b.

Three recirculation regions along the streamwise direction are observed. The first recirculation region is near the leading edge of the upstream body. This region is small in size but the magnitude of the the reverse flow velocity is big. The second recirculation region is observed in the gap between the two bodies. It is anticipated that the recirculation region in this region can be expanded if the gap is made longer to a certain length,[31,32,33] similar to the case of a bluff body with a downstream body arranged in tandem. However, there is still no published data about this critical gap distance except for the case of infinite span length or span with more than one D length. The third region of the recirculation flow is near the trailing edge of the downstream body. This recirculation region is similar to many cases of flow over a bluff body. The length of the recirculation region is about one D.

Figure 7 presents the time-averaged streamwise velocity profile at various locations above the trains surfaces. Experimental data from the hot wire measurements are also plotted for comparison. The data agrees well in the upper region from the point where the velocity start to become constant, i.e, at the boundary layer edge. However, in the near wall region, due to the nature of turbulent modelling near walls that assumes the velocity profile as a logarithmic layer,[34] URANS calculations under predict the velocity magnitude. At the gap, $x = 4.3D$, see Figure 7c, URANS calculations predict the velocity profile very well as there is no boundary layer in that region.

The wake profiles at various downstream locations are shown in Figure 8. The data agree fairly very well, especially near the trailing edge of the downstream body. Further downstream, the URANS calculations produce slow velocity recovery behaviour. A similar condition is also observed by Rodi[35] for the case of flow over a square cylinder using $k - \epsilon$ URANS model. Near the wall, URANS calculations over predict the velocity profile. This probably due to the flow obstruction from the pillars used in the experiment to support

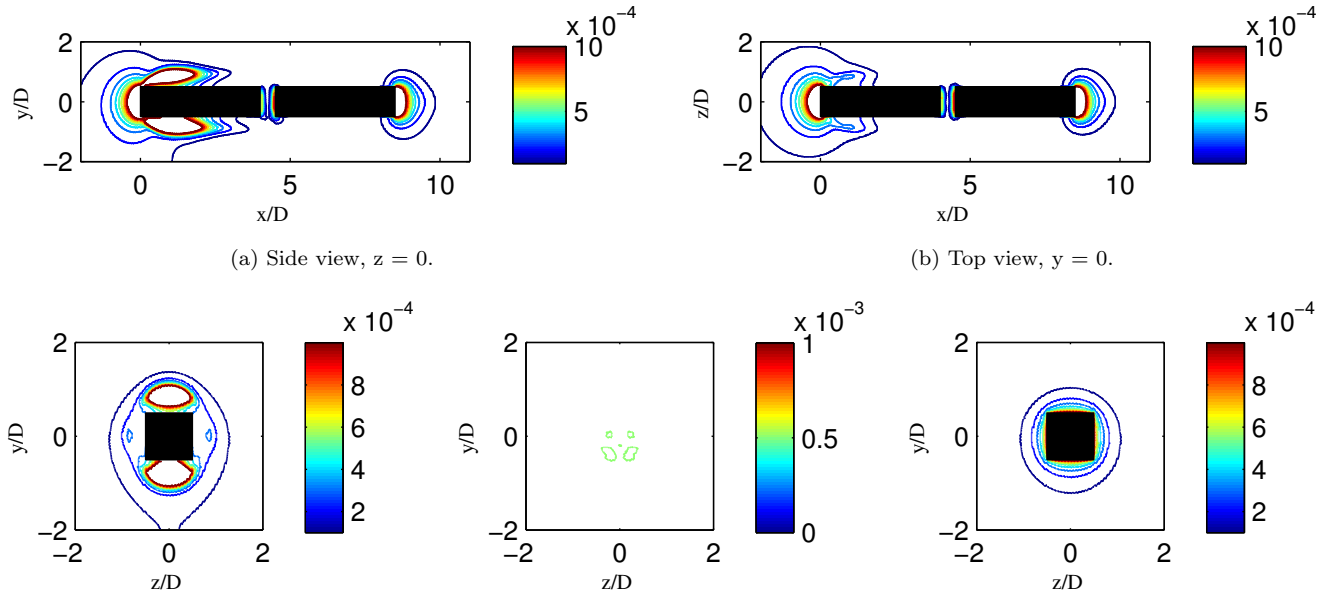

(a) Side view, z = 0.

(b) Top view, y = 0.

(c) Front view, x = D.

(d) Front view, x = 4.25D.

(e) Front view, x = 8.5D.

Figure 5: Root mean square pressure at various selected plane.

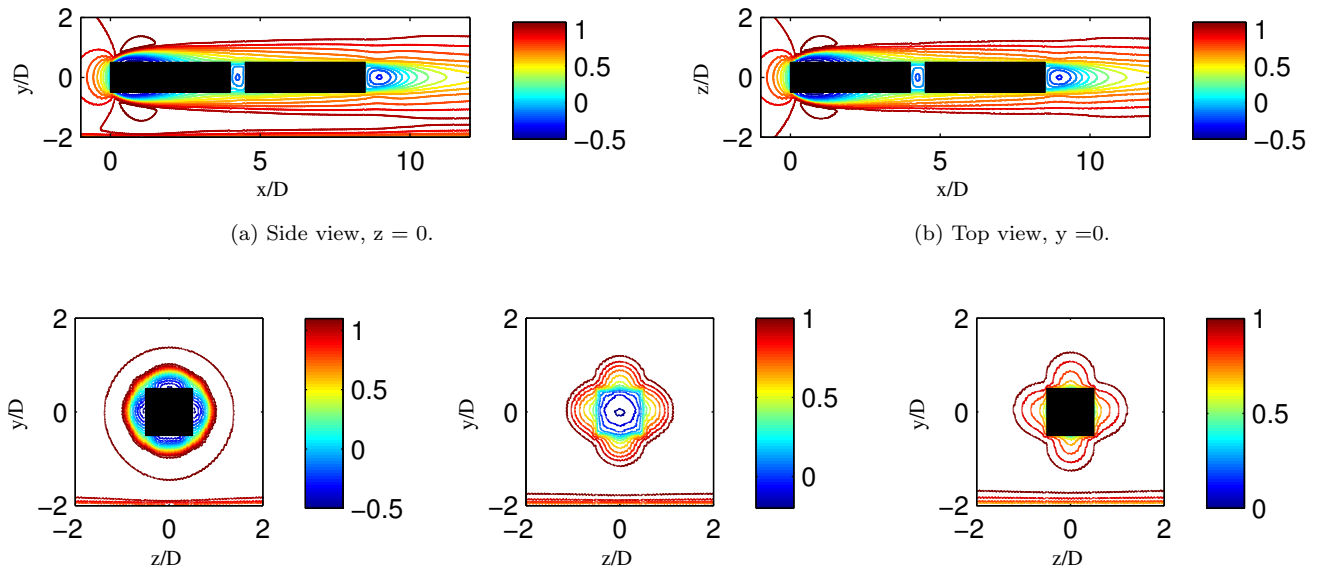

(a) Side view, z = 0.

(b) Top view, y =0.

(c) Front view, x = D.

(d) Front view, x = 4.25D.

(e) Front view, x = 8.5D.

Figure 6: Time-averaged streamwise velocity at various selected plane.

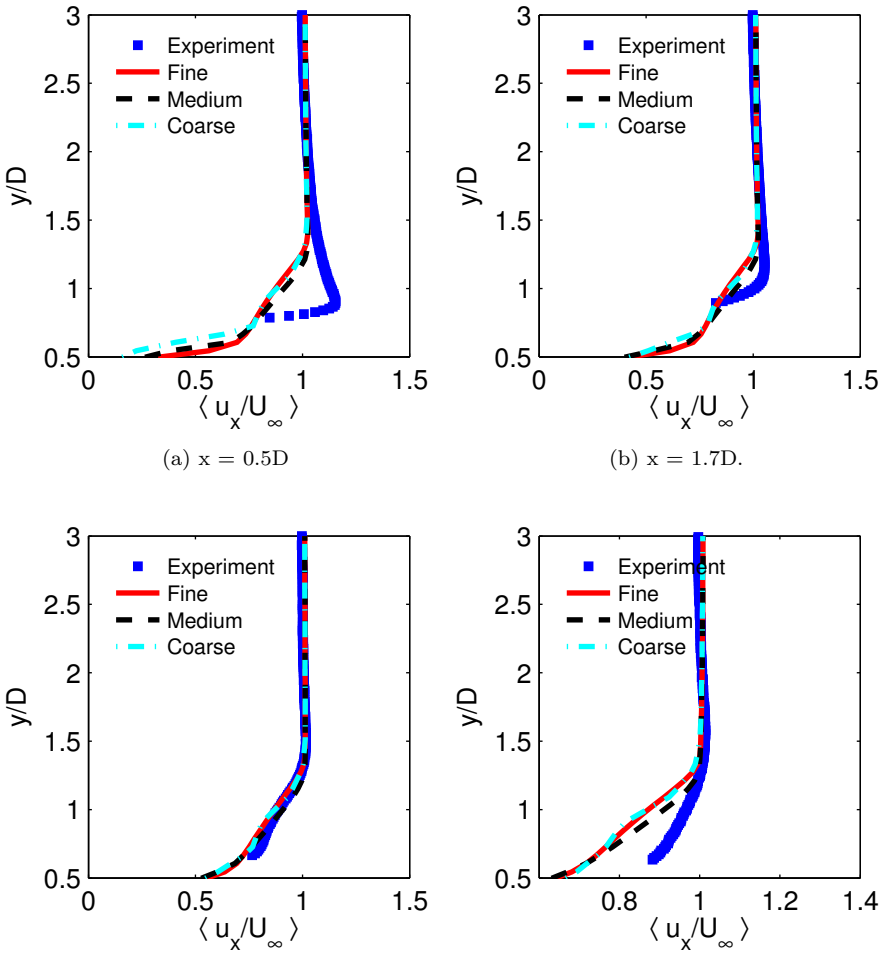

(a) x = 0.5D (b) x = 1.7D.

(c) x = 4.3D. (d) x = 8.4D.

Figure 7: Time-averaged streamwise velocity, $\langle \frac{u_x}{U_\infty} \rangle$, at various streamwise location above the trains surface. Blue-solid line

the model.

Figure 9 shows the distribution of turbulent intensity (Tu= $\sqrt{\frac{2}{3}k}$, where k is the turbulent kinetic energy) at various streamwise locations above the train surfaces. The URANS data is fairly in good agreement with the experiment measurements when a fine mesh is used. Additionally, the turbulent intensity level on the downstream body is lower than the upstream body, see Figures 9c and 9d, due to the lower vortex strength.

Distribution of the turbulent intensity profile in the wake of the trains is shown in Figure 10. URANS calculations under predict the turbulent intensity level when compared with the experiment measurements. The same under perdicted value of the turbulent intensity is also observed from the RANS simulations of flow over a square bluff body of Murukami and Mochida,[36] Lakehal and Rodi[37] and Rodi.[35] Lakehal and Rodi[37] argued that this may be due to the failing of the RANS model to resolve the highly eddy-viscosity physics in the wake flow. Murukami and Mochida[36] suggested using a LES model, and this will be the focus of future work.

B. Acoustics

To demonstrate the effect each of the parameters, nose shape, prism separation, and yaw angle, had on the acoustics, acoustic Power Spectral Density (PSD) plots are shown in Figure 11. These spectra were recorded using microphone 9 of the side array, located at a distance approximately $r = 720\,\text{mm}$ from a point directly above the rear prism, and are processed in the same manner as the beamforming results, as described in D. The results in Figure 11a show that increasing the car spacing causes a significant increase in the measured spectrum, especially between $f = 1$–$3\,\text{kHz}$. The use of a square nose dramatically increases the measured acoustic levels between $f = 0.5$–$2\,\text{kHz}$, as shown in Figure 11b, while increasing the yaw angle increases the acoustic levels for all frequencies above $f = 600\,\text{Hz}$ as shown in Figure 11c.

Beamforming results for a subset of the experiments are presented in Figures 12–15. Figure 12 shows the side-array beamforming results when the car separation is varied. At $f = 2\,\text{kHz}$ the source appears primarily around the nose and tail of the model, with increasing amplitude as the separation distance increases, and at $f = 3.5\,\text{kHz}$ the source is primarily located in the car gap, again with increasing amplitude as the separation distance increases.

Figure 13 shows the results of varying the yaw angle whilst keeping the car separation constant at $1D$ and using the rounded nose. These results correspond to increasing the yaw angle as compared to results in Figures 12c and 12d. At $f = 2\,\text{kHz}$ the sound sources appear to be located around the nose and tail of the model, as per the cases presented in Figure 12 with a small increase in amplitude as the yaw angle increases. Similarly at $f = 3.5\,\text{kHz}$ the source is located at the gap between cars, with increasing amplitude as the yaw angle increases.

The results with different noses and the car separation at $1D$ and 0° yaw are shown in Figure 14. These results correspond to the rounded nose case presented in Figures 12c and 12d. At $f = 2\,\text{kHz}$ the sound sources appear to be at the nose and tail of the train, with small amplitude increases relative to the rounded nose case. At $f = 3.5\,\text{kHz}$ the sound sources are again located in the gap between cars with no appreciable difference in amplitude between all three nose cases.

Finally, results from the top array corresponding to the base case of a rounded nose, $1D$ carriage separation and 0° yaw angle are shown in Figure 15.

IV. Conclusions

Recent results of the fluid dynamics and noise generation around two interacting prisms have been presented. The prisms represent a model HST, and the effect of varying the nose geometry, prism, or carriage, spacing, and yaw angle analysed using a combination of experimental results and CFD.

Results show good agreement between hotwire and CFD results, and future work will compare experimental acoustic results with noise prediction using CFD.

Acoustic results from the interacting prisms show that nose geometry has a large effect at low frequencies, which is also shown in the beamforming results. Increasing prism separation increases sound levels across all frequencies, but most significantly at mid-frequencies, which again agrees well with beamforming results, which show significant noise generation at the gap between prisms at these frequencies. Finally, increasing yaw angle tended to increase noise levels across most frequencies reasonably evenly.

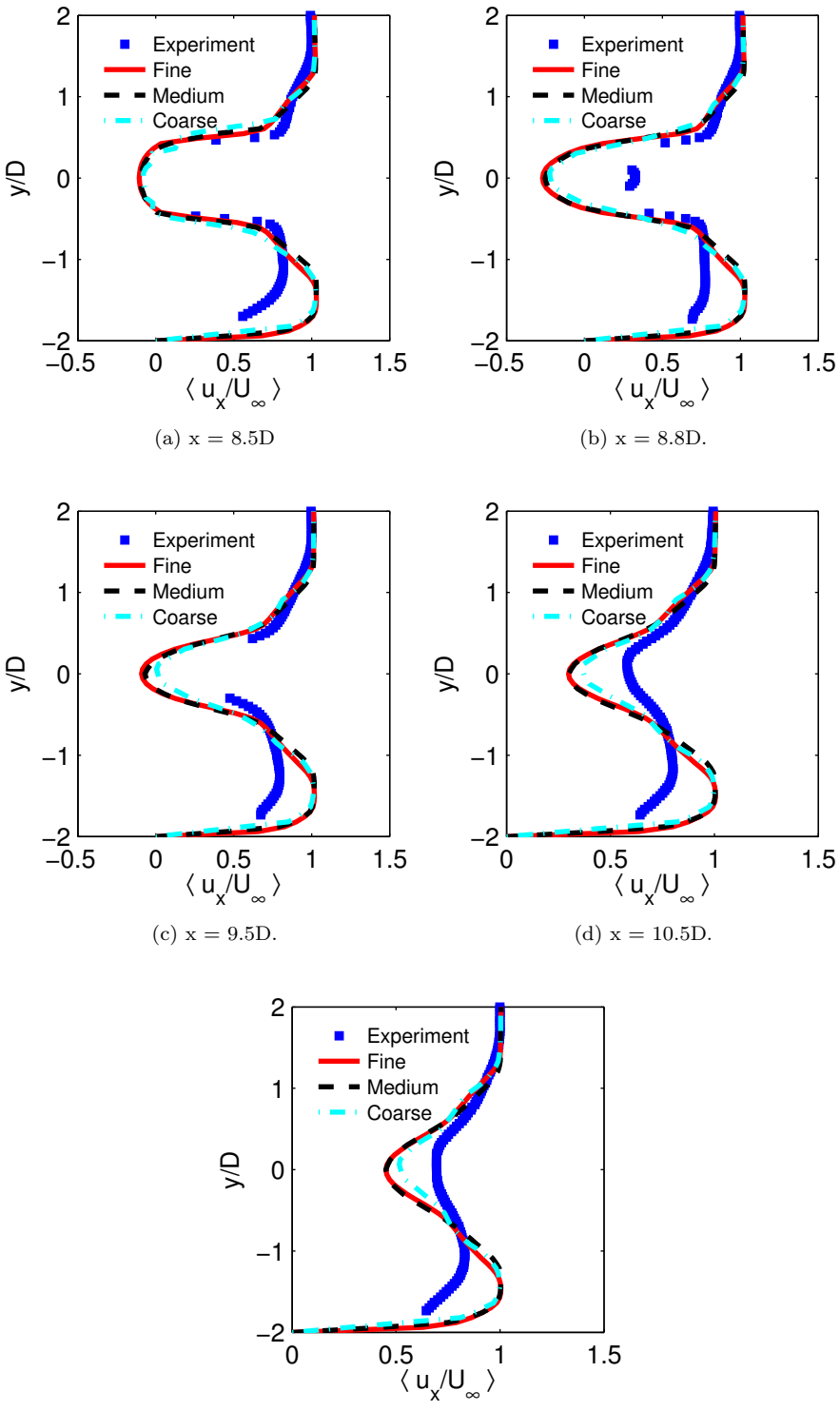

(a) x = 8.5D

(b) x = 8.8D.

(c) x = 9.5D.

(d) x = 10.5D.

(e) x = 11.5D.

Figure 8: Time-averaged streamwise velocity, $\langle \frac{u_x}{U_\infty} \rangle$, at various locations in the wake.

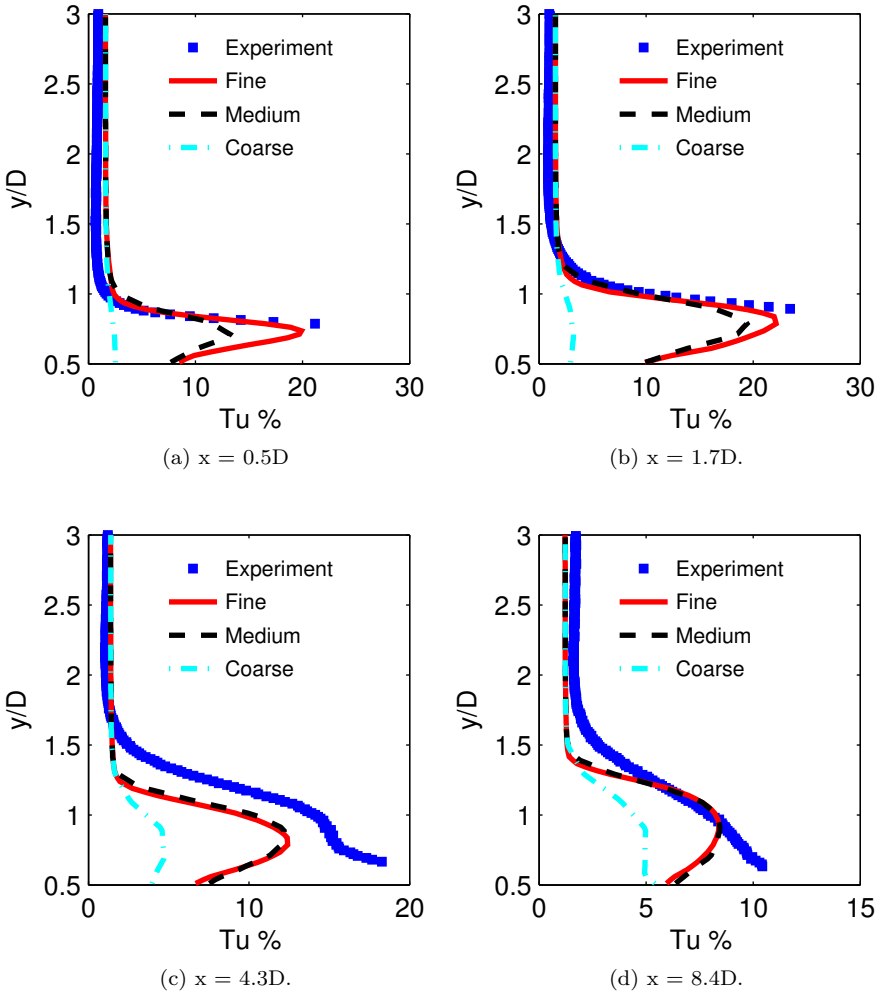

(a) x = 0.5D (b) x = 1.7D.

(c) x = 4.3D. (d) x = 8.4D.

Figure 9: Turbulent intensity (Tu%) at various location above the trains surface.

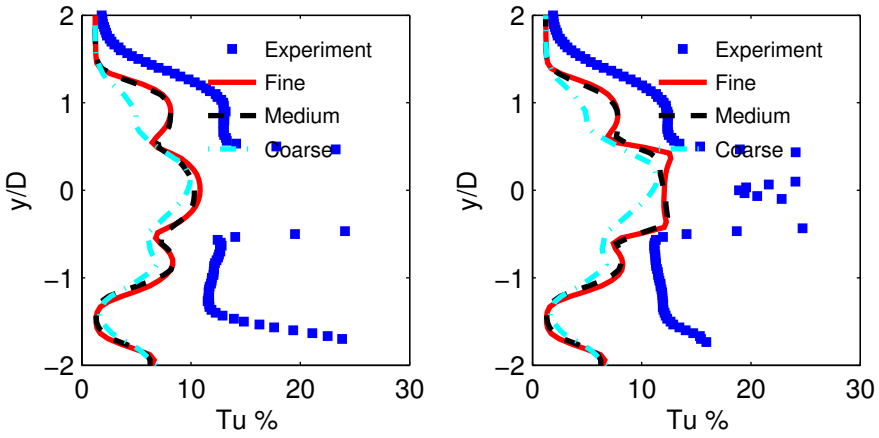

(a) x = 8.5D

(b) x = 8.8D.

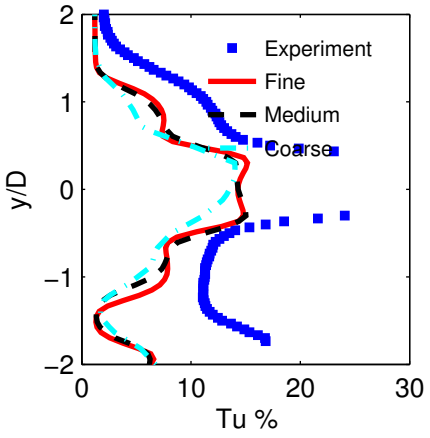

(c) x = 9.5D.

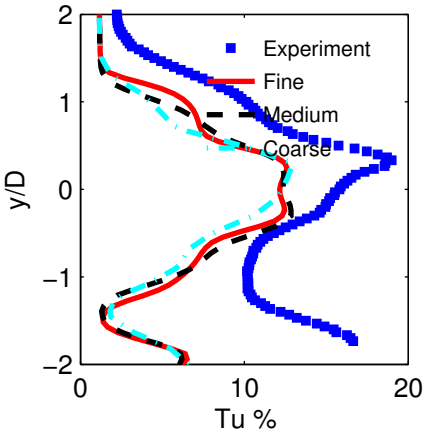

(d) x = 10.5D.

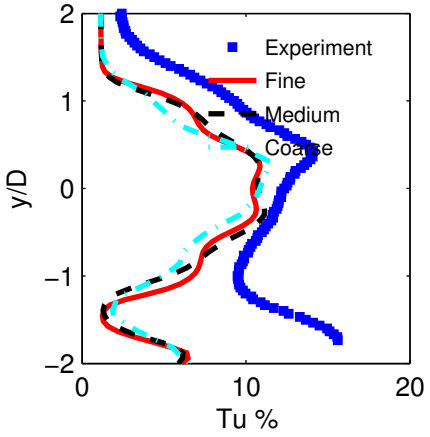

(e) x = 11.5D.

Figure 10: Turbulent intensity at various locations in the wake.

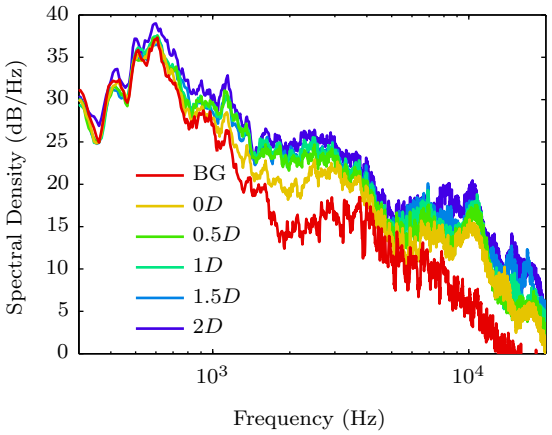

(a) Varying car separation.

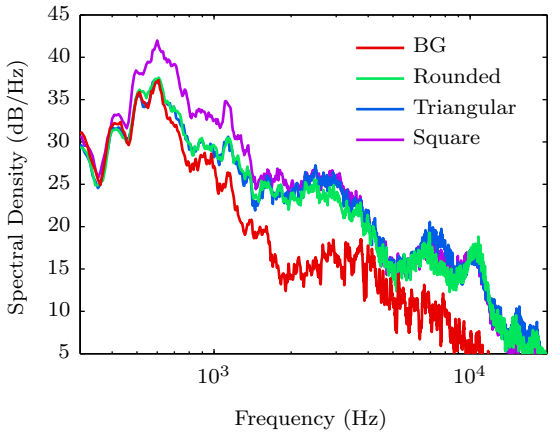

(b) Varying nose type.

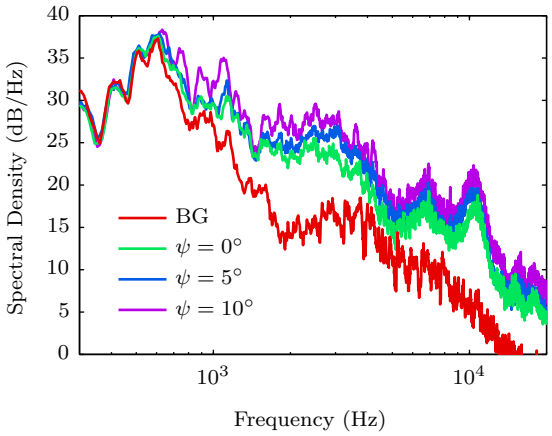

(c) Varying yaw angle.

Figure 11: Single microphone acoustic spectra when varying one of the test parameters. The results shown are for the rounded nose, car separation of 15 mm, and a 0° yaw angle (ψ) unless it is the parameter being varied. In all figures, BG refers to the background level recorded with the wind tunnel on and the side plate mounted without the train model.

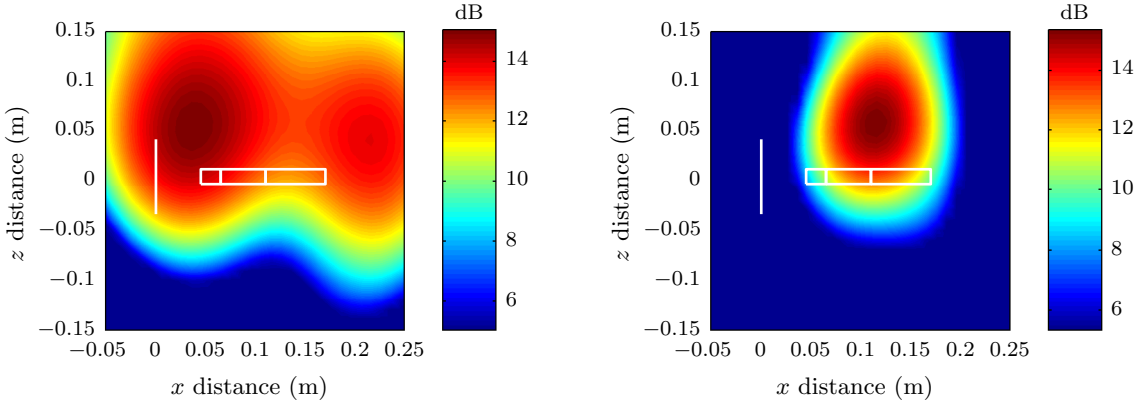

(a) $0D$ car separation, $f = 2000\,\mathrm{Hz}$

(b) $0D$ car separation, $f = 3496\,\mathrm{Hz}$

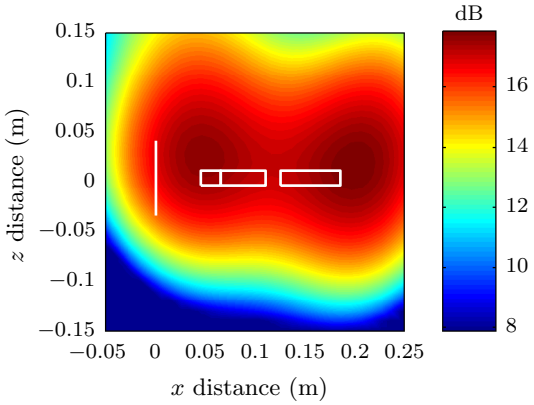

(c) $1D$ car separation, $f = 2000\,\mathrm{Hz}$

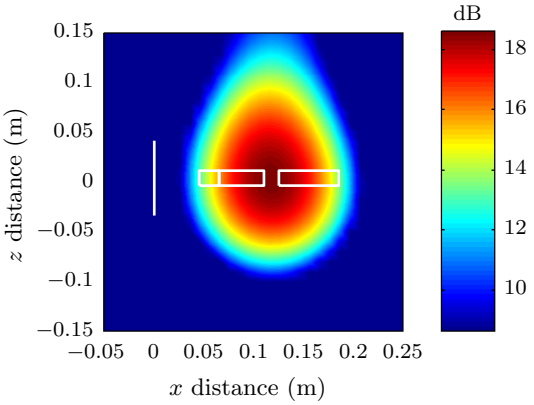

(d) $1D$ car separation, $f = 3496\,\mathrm{Hz}$

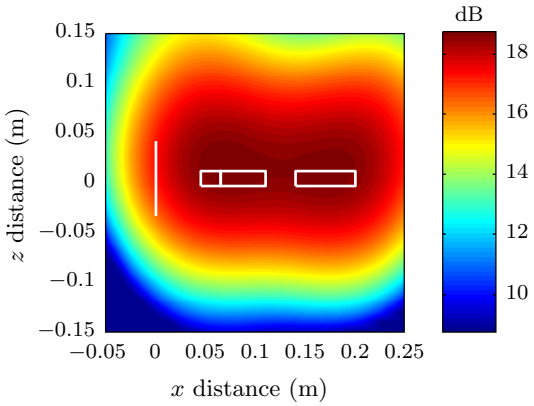

(e) $2D$ car separation, $f = 2000\,\mathrm{Hz}$

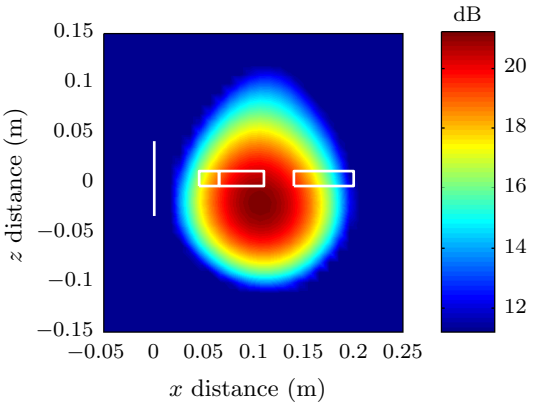

(f) $2D$ car separation, $f = 3496\,\mathrm{Hz}$

Figure 12: Side-array beamforming results for the train model with the rounded nose, 0° yaw and varying car separation. The vertical white line shows the position of the wind tunnel outlet.

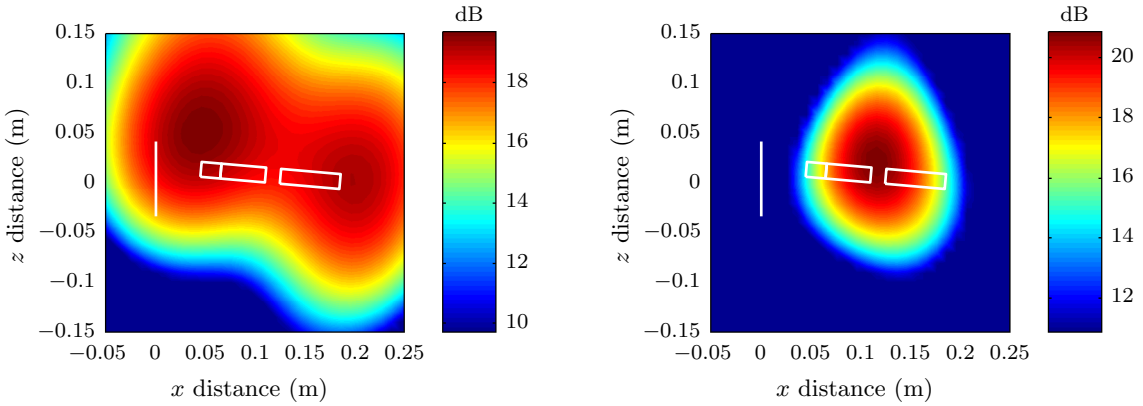

(a) 5° yaw angle, $f = 2000\,\text{Hz}$

(b) 5° yaw angle, $f = 3496\,\text{Hz}$

(c) 10° yaw angle, $f = 2000\,\text{Hz}$

(d) 10° yaw angle, $f = 3496\,\text{Hz}$

Figure 13: Side-array beamforming results for the train model with the rounded nose, $1D$ car separation and varying yaw angles. The vertical white line shows the position of the wind tunnel outlet.

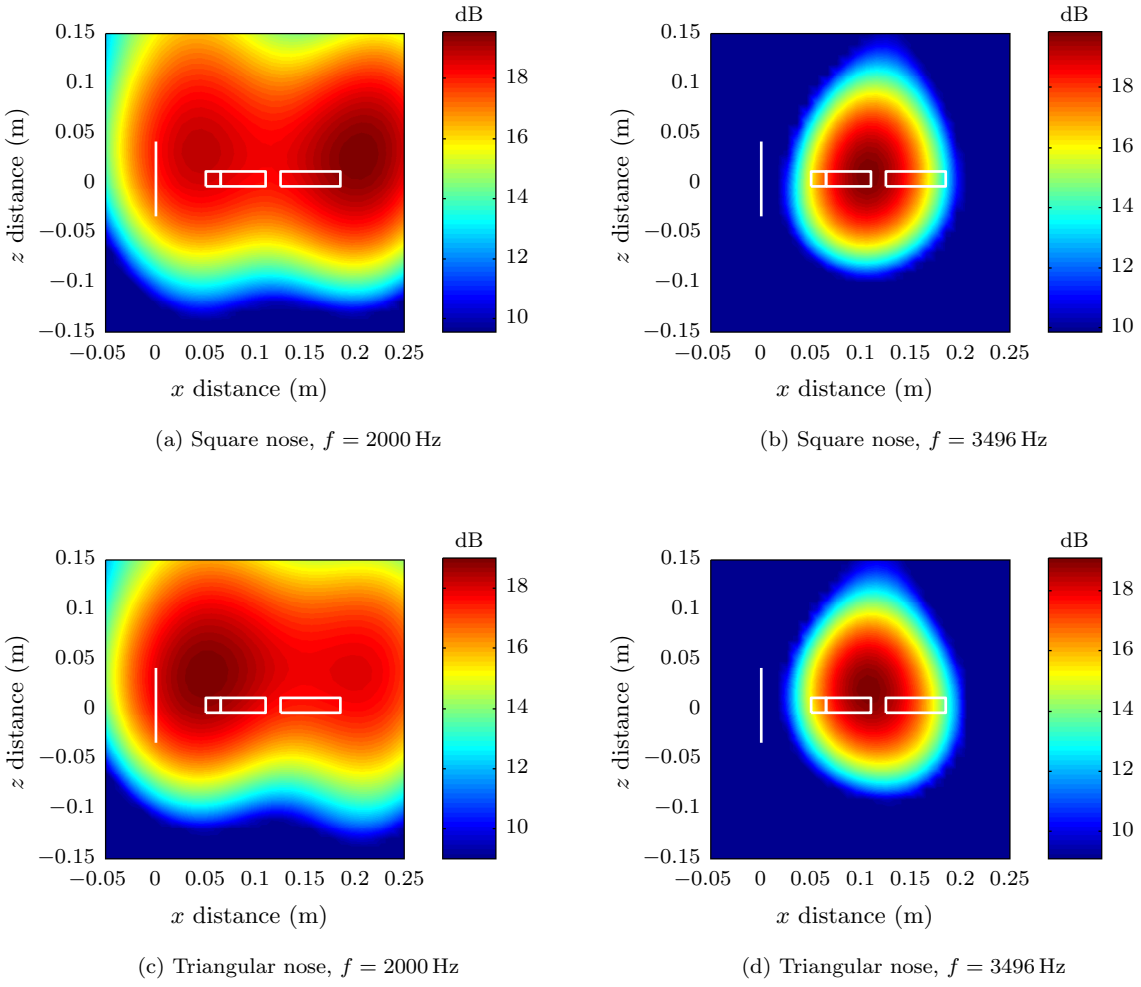

(a) Square nose, $f = 2000\,\text{Hz}$

(b) Square nose, $f = 3496\,\text{Hz}$

(c) Triangular nose, $f = 2000\,\text{Hz}$

(d) Triangular nose, $f = 3496\,\text{Hz}$

Figure 14: Side-array beamforming results for the the train model for $1D$ car separation, 0° yaw angle and different nose shapes. The vertical white line shows the position of the wind tunnel outlet.

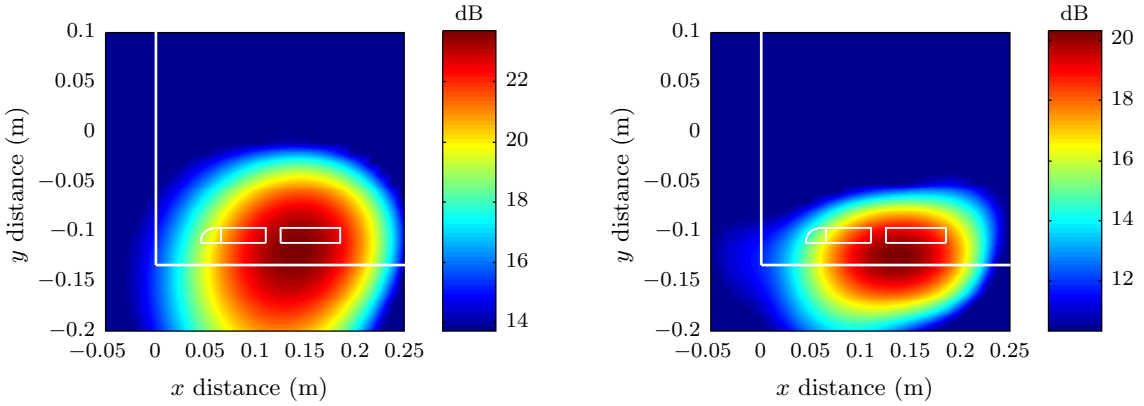

(a) Top results corresponding to Figure 12c.

(b) Top results corresponding to Figure 12d.

Figure 15: Top-array beamforming results for the train model corresponding to the nominal test case of a rounded nose, 0° yaw and 1D car separation. The horizontal white line shows the location of the plate, and the vertical white line shows the position of the wind tunnel outlet.

Acknowledgements

This work was supported by a research grant from the Australia-Malaysia Institute.

References

[1]Givoni, M., "Development and Impact of the Modern High-speed Train: A Review," *Transport reviews*, Vol. 26, No. 5, 2006, pp. 593–611.

[2]Sagawa, A., Ono, S., Hidetoshi, H., and Aso, T., "Aeroacoustic noise generated from high-speed trains in Japan," *5th AIAA/CEAS Aeroacoustics Conference*, Bellevue, WA, USA, 10–12 May, 1999.

[3]Takaishi, T., Sagawa, A., and Nagakura, K., "Numerical analysis of dipole sound source around high speed trains," *40th AIAA Aerospace Sciences Meeting & Exhibit*, Reno, NV, USA, 14–17 January, 2002.

[4]Talotte, C., "Aerodynamic noise: a critical survey," *Journal of Sound and Vibration*, Vol. 231, No. 3, 2000, pp. 549–562.

[5]Baker, C., Cheli, F., Orellano, A., Paradot, N., Proppe, C., and Rocchi, D., "Cross-wind effects on road and rail vehicles," *Vehicle system dynamics*, Vol. 47, No. 8, 2009, pp. 983–1022.

[6]Chiu, T. and Squire, L., "An experimental study of the flow over a train in a crosswind at large yaw angles up to 90," *Journal of Wind Engineering and Industrial Aerodynamics*, Vol. 45, No. 1, 1992, pp. 47–74.

[7]Copley, J., "The three-dimensional flow around railway trains," *Journal of Wind Engineering and Industrial Aerodynamics*, Vol. 26, No. 1, 1987, pp. 21–52.

[8]Suzuki, M., Tanemoto, K., and Maeda, T., "Aerodynamic characteristics of train/vehicles under cross winds," *Journal of Wind Engineering and Industrial Aerodynamics*, Vol. 91, No. 1, 2003, pp. 209–218.

[9]Hoppmann, U., Koenig, S., Tielkes, T., and Matschke, G., "A short-term strong wind prediction model for railway application: design and verification," *Journal of wind engineering and industrial aerodynamics*, Vol. 90, No. 10, 2002, pp. 1127–1134.

[10]Cooper, R., "The effect of cross-winds on trains," *Journal of Fluids Engineering*, Vol. 103, No. 1, 1981, pp. 170–178.

[11]Peters, J., "Aerodynamics of very high speed trains and maglev vehicles: State of the art and future potential," *Int. J. of Vehicle Design, Special Publication Sp3*, 1983.

[12]Krajnovic, S., Hemida, H., and Diedrichs, B., "Time-dependent simulations for the directional stability of high speed trains under the influence of cross winds or cruising inside tunnels," *FLUID DYNAMICS APPLICATIONS IN GROUND TRANSPORTATION: Simulation, a primary delepment tool in the automotive industry, Lyon, France, 26-27 October 2005*, 2005.

[13]Mellet, C., Ĺtourneaux, F., Poisson, F., and Talotte, C., "High speed train noise emission: Latest investigation of the aerodynamic/rolling noise contribution," *Journal of sound and vibration*, Vol. 293, No. 3, 2006, pp. 535–546.

[14]WARIS, M. B., ISHIHARA, T., SARWAR, M. W., and FUJINO, Y., "Numerical study of aerodynamic forces on trains in crosswind using LES turbulence model," .

[15]Hemida, H. and Krajnović, S., "LES study of the influence of a train-nose shape on the flow structures under cross-wind conditions," *Journal of Fluids Engineering*, Vol. 130, No. 9, 2008, pp. 091101.

[16]Lauterbach, A., Ehrenfried, K., Loose, S., and Wagner, C., "Scaling of Aeroacoustic Sources Measured on High-Speed Trains," *17th AIAA/CEAS Aeroacoustics Conference (32nd AIAA Aeroacoustics Conference)*, Portland, OR, USA, 2011.

[17]King III, W. F. and Bechert, D., "On the sources of wayside noise generated by high-speed trains," *Journal of Sound and Vibration*, Vol. 66, No. 3, 1979, pp. 311–332.

[18]Menter, F. R., "Two-equation eddy-viscosity turbulence models for engineering applications," *AIAA journal*, Vol. 32, No. 8, 1994, pp. 1598–1605.

[19]Jasak, H., *Error analysis and estimation for the finite volume method with applications to fluid flows*, Ph.D. thesis, Department of Mechanical Engineering, Imperial College of Science, Technology and Medicine, June 1996.

[20]Leonard, B. P., "A stable and accurate convective modelling procedure based on quadratic upstream interpolation," *Computer Methods in Applied Mechanics and Engineering*, Vol. 19, No. 1, 1979, pp. 59 – 98.

[21]Courant, R., Friedrichs, K., and Lewy, H., "On the partial difference equations of mathematical physics," *IBM J. Res. Dev.*, Vol. 11, No. 2, 1967, pp. 215–234.

[22]Weller, H. G., Tabor, G., Jasak, H., and Fureby, C., "A tensorial approach to computational continuum mechanics using object-oriented techniques," *Computers in Physics*, Vol. 12, No. 6, 1998, pp. 620–631.

[23]Moreau, D. J., Brooks, L. A., and Doolan, C. J., "Broadband trailing edge noise from a sharp-edged strut," *The Journal of the Acoustical Society of America*, Vol. 129, No. 5, 2011, pp. 2820–2829.

[24]Underbrink, J. R., "Aeroacoustic Phased Array Testing in Low Speed Wind Tunnels," *Aeroacoustic Measurements*, edited by T. J. Mueller, chap. 3, Springer, Berlin, 2002, pp. 98–217.

[25]Johnson, D. H. and Dudgeon, D. E., *Array Signal Processing: Concepts and Techniques*, Prentice Hall, Upper Saddle River, NJ, USA, 1993.

[26]Dougherty, R. P., "Beamforming in Acoustic Testing," *Aeroacoustic Measurements*, edited by T. J. Mueller, chap. 2, Springer, Berlin, 2002, pp. 62–97.

[27]Padois, T., Prax, C., and Valeau, V., "Numerical validation of shear flow corrections for beamforming acoustic source localisation in open wind-tunnels," *Applied Acoustics*, Vol. 74, No. 4, 2013, pp. 591–601.

[28]Ali, M. S. M., Doolan, C. J., and Wheatley, V., "Low Reynolds number flow over a square cylinder with a splitter plate," *Physics of Fluids*, Vol. 23, No. 3, 2011, pp. 033602.

[29]Ali, M. S. M., Doolan, C. J., and Wheatley, V., "Low Reynolds number flow over a square cylinder with a detached flat plate," *International Journal of Heat and Fluid Flow*, Vol. 36, 2012, pp. 133–141.

[30]Hourigan, K., Thompson, M., and Tan, B., "Self-sustained oscillations in flows around long blunt plates," *Journal of Fluids and Structures*, Vol. 15, No. 3, 2001, pp. 387–398.

[31]Leclercq, D. J. J. and Doolan, C. J., "The interaction of a bluff body with a vortex wake," *Journal of Fluids and Structures*, Vol. 25, No. 5, 2009, pp. 867–888.

[32]Ali, M. S. M., Doolan, C. J., and Wheatley, V., "The sound generated by a square cylinder with a splitter plate at low Reynolds number," *Journal of Sound and Vibration*, Vol. 330, No. 15, 2011, pp. 3620–3635.

[33]Ali, M. S. M., Doolan, C. J., and Wheatley, V., "Aeolian Tones Generated by a Square Cylinder with a Detached Flat Plate," *AIAA Journal*, Vol. 51, No. 2, 2013, pp. 291–301.

[34]Kalitzin, G., Medic, G., Iaccarino, G., and Durbin, P., "Near-wall behavior of RANS turbulence models and implications for wall functions," *Journal of Computational Physics*, Vol. 204, No. 1, 2005, pp. 265–291.

[35]Rodi, W., "Comparison of LES and RANS calculations of the flow around bluff bodies," *Journal of Wind Engineering and Industrial Aerodynamics*, Vol. 69, 1997, pp. 55–75.

[36]Murakami, S. and Mochida, A., "On turbulent vortex shedding flow past 2D square cylinder predicted by CFD," *Journal of Wind Engineering and Industrial Aerodynamics*, Vol. 54, 1995, pp. 191–211.

[37]Lakehal, D. and Rodi, W., "Calculation of the flow past a surface-mounted cube with two-layer turbulence models," *Journal of Wind Engineering and Industrial Aerodynamics*, Vol. 67, 1997, pp. 65–78.